Rotational symmetry breaking on the Rydberg energy spectrum of indirect excitons in diamond studied by terahertz time-domain spectroscopy

T. Ichii,[1,*] N. Naka,[1] and K. Tanaka[1,2,†]

[1]*Department of Physics, Kyoto University, Kyoto 606-8502, Japan*

[2]*Institute for Integrated Cell-Material Sciences (WPI-iCeMS), Kyoto University, Kyoto 606-8501, Japan*

(Received 22 September 2021; accepted 23 September 2021; published 3 November 2021)

We investigated the 1*S*-2*P* transitions of the indirect excitons in diamond around 70 meV in the high-frequency terahertz region via time-resolved Lyman spectroscopy. We discovered significant splitting of the 2*P* levels and attributed it to the rotational-symmetry-breaking effect owing to the cubic crystal environment. The maximum energy separation of 14.9 meV reached 18% of the excitonic Rydberg constant—83.5 ± 2.9 meV—which deviated from the binding energy of the 1*S* ground state: 93.3 ± 2.0 meV. In addition to the anisotropy of the valence bands, we found the impact of the rotational symmetry breaking of the conduction band valleys, which leads to a significant deviation from the case with direct excitons. Detailed knowledge of the ground and excited states of long-lifetime excitons provides an unprecedented opportunity to develop the study of quantum many-body physics and quantum chaos.

DOI: 10.1103/PhysRevB.104.205201

I. INTRODUCTION

In semiconductors, photo-excitations above the band gap create a negatively charged electron in the conduction band and a positively charged hole in the valence band. The Coulomb attraction between the electron and hole leads to the formation of the bound state known as an exciton [1]. Because of similar energy structure [2], excitons have gained attention as an analogue of the hydrogen atom in crystals. The hydrogenlike description has motivated the use of excitonic ground states toward the realization of Bose-Einstein condensations [3] and the highly excited (Rydberg) states for the study of quantum chaos [4]. However, there is an inherent difference between hydrogen and exciton.

For hydrogen, the Hamiltonian with the Coulomb potential is invariant under three-dimensional rotations. The Runge-Lenz vector is conserved owing to the $1/r$ dependence of the Coulomb potential at a distance r. Conservation signifies the existence of the hidden symmetry, called *dynamical symmetry* [5], and causes degeneracy in the orbital angular momentum L with symmetry of SO(4) for nonrelativistic hydrogen. The energy levels and a typical wave function are shown in Fig. 1(a). We note that, for relativistic hydrogen, the spin-orbit interaction breaks the dynamical symmetry. The continuous rotational symmetry of SO(3) leads to energy splitting in L, keeping the degeneracy in L_z; that is the z component of L. The energy levels are split with respect to L [6], while the rotational symmetry is preserved in the absence of external fields.

For an exciton, both the dynamical and rotational symmetries are broken by crystal environments. Here, L and L_z are no longer good quantum numbers, giving rise to further level splits. Hitherto, Coulomb-bound pairs in crystals have been extensively studied using an acceptor hole or donor electron, weakly bound to an impurity potential [7]. In the effective-mass approach, such impurity states are described by the Hamiltonian for a hole or electron moving with an effective mass in the Coulomb potential [7]. If the energy bands determining the effective masses were anisotropic in the reciprocal space because of the lower symmetry of the crystal than that of the Coulomb potential, the dynamical and rotational symmetries of the Hamiltonian are broken. Then the energy levels and eigenfunctions, called *envelope functions*, deviate from those of hydrogen [Fig. 1(b)].

The excitonic states are described by the Hamiltonian for the Coulomb-bound pair of holes and electrons having different and anisotropic effective masses. The anisotropy contributes to the additional symmetry breaking, leading to a more complicated level splitting shown in Fig. 1(c) than that in Fig. 1(b). Despite theoretical prediction [8], such a specific but miniscule deviation expected for excitons in indirect semiconductors has been technically challenging to observe [9,10]. We note that a deviation of excitonic levels from the relativistic hydrogen model has been reported in a direct semiconductor of cuprous oxide owing to the state-of-the-art high-resolution technique and the relatively large excitonic binding energy [11]. However, because of the isotropic electron effective mass, the symmetry breaking in cuprous oxide is inherently like that in the case of an acceptor hole.

Here, we focused on a wide-gap indirect semiconductor of diamond for the observation of unprecedented symmetry-breaking effects on the Rydberg energy spectrum of excitons. Unlike conventional indirect semiconductors, diamond has an exceptionally high exciton binding energy E_b of ∼80 meV [12]. This unique property paves the way to resolve the level splitting directly using a spectroscopy method because the

*tichii@ims.ac.jp

†kochan@scphys.kyoto-u.ac.jp

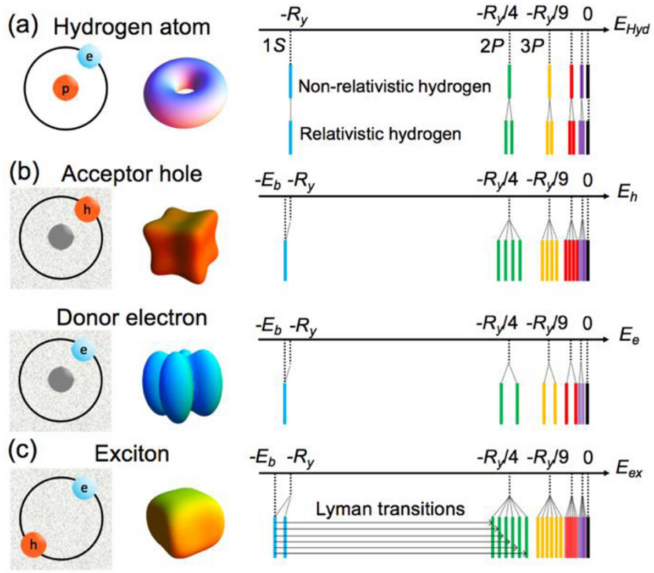

FIG. 1. Contour plots of the wave function of a $2P$ state and the energy series for (a) nonrelativistic and relativistic hydrogen, (b) impurity states, and (c) exciton. The binding energy in the lowest $1S$ level E_b does not necessarily coincide with the Rydberg constant R_y. The splitting in the $2P$ states is directly observed through the Lyman transitions, as indicated by arrows.

level splitting varies proportionally to the Rydberg constant [8]. Hitherto, photoluminescence measurements revealed that symmetry breaking is crucial in the splitting of excitonic ground states [13]. However, excitonic excited levels remain elusive because of their weak photoluminescence intensities owing to the fast relaxation to the ground states.

Recently, we developed a pump-probe spectroscopy system with a broadband terahertz pulse to investigate the $1S$-nP (Lyman) transitions in diamond [14]. Time-resolved Lyman spectroscopy is a powerful tool for studying excitonic excited levels [15,16]. The method uses a pump pulse to create excitons and monitors the Lyman transitions with a time-delayed probe pulse. At the delay time, when excitons are relaxed in the ground state, we can observe the splitting in the excited $2P$ states in the absorption of the probe pulse [Fig. 1(c)]. Using this system, we successfully observed significant deviations in $2P$ levels from the Rydberg series. Based on the effective-mass approach, we found that level splitting is caused by the breaking of the continuous rotational symmetry due to anisotropy in both the valence and conduction bands. This leads to the observed significant deviation from the case of direct semiconductors. Furthermore, we determined the values of the Rydberg constant and binding energy of excitons in diamond.

The remainder of this paper is structured as follows. We explain the Hamiltonian and rotational symmetry breaking of diamond excitons in Sec. II. Section III describes the sample and experimental setup of the pump-probe spectroscopy system with a terahertz pulse. In Sec. IV, we present observations of the four-level splitting of $2P$ states for indirect excitons in diamond. We demonstrate the signature of the rotational symmetry breaking and discuss the significant effects of anisotropy on the valence and conduction bands for level splitting. Section V concludes this paper.

II. THEORY

Throughout this paper, we use the notations by Koster *et al.* [17]. Diamond has a cubic crystal structure with O_h symmetry. The valence band maximum located at the Γ point belongs to the representation of Γ_5^+ of the O_h point group. The valence band has a threefold degeneracy owing to the P-like orbital part. Owing to the spin-orbit interaction ($E_{\rm so}$), the band splits into twofold $J=\frac{1}{2}$ and fourfold $J=\frac{3}{2}$ bands, where J is the total angular momentum of the hole. We note that $J_z=\pm\frac{1}{2}$ and $\pm\frac{3}{2}$ bands show different energy dispersion [18]. Meanwhile, the conduction band, originating from the S-like orbital, takes the energy minimum at the six equivalent Δ points, which belongs to the representation of Δ_1 of the C_{4v} group. The valence and conduction bands are anisotropic. Here, we ignore the electron spin because we are concerned with the $2P$ levels with negligible exchange interactions [19]. When the Rydberg constant R_y and Bohr radius are, respectively, taken as units of energy and length, following Dresselhaus [20], the effective-mass Hamiltonian for the exciton is described by the Rydberg Hamiltonian with four perturbative terms [8]:

$$H_{\rm ex}=\left(\frac{p^2}{\hbar^2}-\frac{2}{r}\right)+H_{\rm so}+H_{\rm sph}+H_{\rm cubic}+H_{\rm EMA}, \qquad (1)$$

where $H_{\rm so}$ represents the spin-orbit interaction in the valence band, which gives rise to the splitting with respect to J. Here, r and p are the relative electron-hole coordinate and momentum, respectively. The spherical term $H_{\rm sph}$ gives different isotropic energy dispersions for $J_z=\pm\frac{1}{2}$ and $\pm\frac{3}{2}$ in the $J=\frac{3}{2}$ band. The cubic term $H_{\rm cubic}$ with O_h symmetry and the electron mass anisotropy term $H_{\rm EMA}$ with $D_{\infty h}$ symmetry come from the anisotropy in the valence and conduction bands, respectively. If $H_{\rm cubic}$ and $H_{\rm EMA}$ are removed, $H_{\rm ex}$ may maintain SO(3) symmetry.

The terms $H_{\rm so}$, $H_{\rm sph}$, $H_{\rm cubic}$, and $H_{\rm EMA}$ are described as follows [8]:

$$H_{\rm so}=\frac{2}{3}\bar{\Delta}(1+\mathbf{J}\cdot\boldsymbol{s_h}),$$

$$H_{\rm sph}=-\frac{\mu}{9\hbar^2}[P^{(2)}\cdot J^{(2)}],$$

$$H_{\rm cubic}=\frac{\delta}{9\hbar^2}\left\{\sum_{k=4,-4}[P^{(2)}\cdot J^{(2)}]_k^4+\frac{\sqrt{70}}{5}[P^{(2)}\cdot J^{(2)}]_0^4\right\},$$

$$H_{\rm EMA}=-\mu_{01}\left(\frac{2}{3}\right)^{1/2}\frac{1}{\hbar^2}P_0^{(2)},$$

where $\bar{\Delta}=E_{\rm so}/R_y$ is the dimensionless spin-orbit splitting, $\boldsymbol{s_h}$ is the hole spin operator ($s_h=\frac{1}{2}$), and $\mathbf{J}$ is the angular momentum operator of the P-like valence band. Here, $P_q^{(2)}$ and $J_q^{(2)}$ ($q=-2,-1,0,1,2$) are the irreducible components of the second-rank Cartesian tensor operators P_{ij} and J_{ij}, which are defined as $P_{ij}=3p_ip_k-\delta_{ik}p^2$, $J_{ij}=\frac{3}{2}(J_iJ_k+J_kJ_j)-\delta_{ik}J^2$ ($i,j=x,y,z$). The coefficients μ, δ, and μ_{01} represent the interaction strengths of $H_{\rm sph}$, $H_{\rm cubic}$, and $H_{\rm EMA}$, respectively [8]. They are expressed as

$\mu = (6\gamma_3 + 4\gamma_2)\mu_{ex}/5m_0$, $\delta = (\gamma_3 - \gamma_2)\mu_{ex}/m_0$, and $\mu_{01} = \mu_{ex}(1/m_t - 1/m_l)/3$, where $\frac{1}{\mu_{ex}} = \frac{1}{3}(\frac{2}{m_t} + \frac{1}{m_l}) + \frac{\gamma_1}{m_0}$, m_0 is free electron mass, γ_i $(i = 1, 2, 3)$ are the Luttinger parameters [21], and $m_t(m_l)$ is the transverse (longitudinal) electron mass, respectively. The matrix form of H_{ex} in Eq. (1) is shown in Appendices A and B. In addition, the difference in momentum between the valence band maximum and conduction band minimum is ignored for approximation purposes [22].

III. EXPERIMENTS

We used a 500-μm-thick chemical-vapor-deposition diamond (Element Six), with nitrogen (<5 ppb) and boron (<1 ppb) as unintentionally incorporated dopants. Our experiment is based on near-infrared laser pulses from a Ti:sapphire amplifier operating at a 1 kHz repetition rate, which delivered 7 mJ pulses with a 35 fs duration. The fundamental pulse (800 nm wavelength) was split into three beams: one for a deep ultraviolet (DUV) pump to generate excitons, and two for the terahertz generation and detection. The DUV pulses at 267 nm, prepared by third-harmonic generation, homogeneously created transient free carriers through the sample at a density of the order of $n_{eh} = 10^{15}\,\mathrm{cm}^{-3}$ via a two-photon absorption process [23]. The excitation condition was the same as in the previous study [14]. We used a collinear air plasma method for the generation of a broadband terahertz pulse (8–110 meV) [14,24]. The terahertz pulse focused on the sample irradiated with the DUV pulse. The spot diameter of the terahertz pulse was 140 μm measured using a terahertz camera (NEC IRV-T0831). The beam size of the excitation pulse was 1.0 mm. The terahertz pulse transmitted through the sample with and without the DUV pulse was detected by an air biased coherent detection [14,25]. We obtained the complex transmittance change by Fourier transformation of the waveform and estimated the photo-induced change in the complex relative dielectric function $\delta\varepsilon = \delta\varepsilon_1 + i\delta\sigma_1/\varepsilon_0\omega$, where $\delta\sigma_1$ is the change in the real part of the optical conductivity and ε_0 is the vacuum permittivity.

IV. RESULTS AND DISCUSSION

A. Observation of the splitting in 2*P* levels via Lyman transitions

Figures 2(a) and 2(b) show the photo-induced change of $\delta\varepsilon_1$ and $\delta\sigma_1$, respectively, at various delay times for a 13 K lattice temperature. We observed the Drude response of the photo-excited free carriers at $\Delta t = 10$ ps, as is expected from the excitation condition. The spectral response in the lower-frequency region is reproduced by the Drude model:

$$\delta\varepsilon_1(\omega) = -\frac{n_{eh}e^2}{\varepsilon_0 m^*}\frac{1}{(\omega^2 + {\gamma_{eh}}^2)},$$
$$\delta\sigma_1(\omega) = \frac{n_{eh}e^2}{m^*}\frac{\gamma_{eh}}{(\omega^2 + {\gamma_{eh}}^2)}, \quad (2)$$

where γ_{eh} is the damping constant, and $m^* = (1/m_e + 1/m_h)^{-1} = 0.19m_0$ [18] is the exciton reduced mass. The best fit [red solid lines in Figs. 2(a) and 2(b)] yielded $n_{eh} = 4.0 \times 10^{15}\,\mathrm{cm}^{-3}$. At this low carrier density, no many-particle effects, such as the formation of polyexcitons

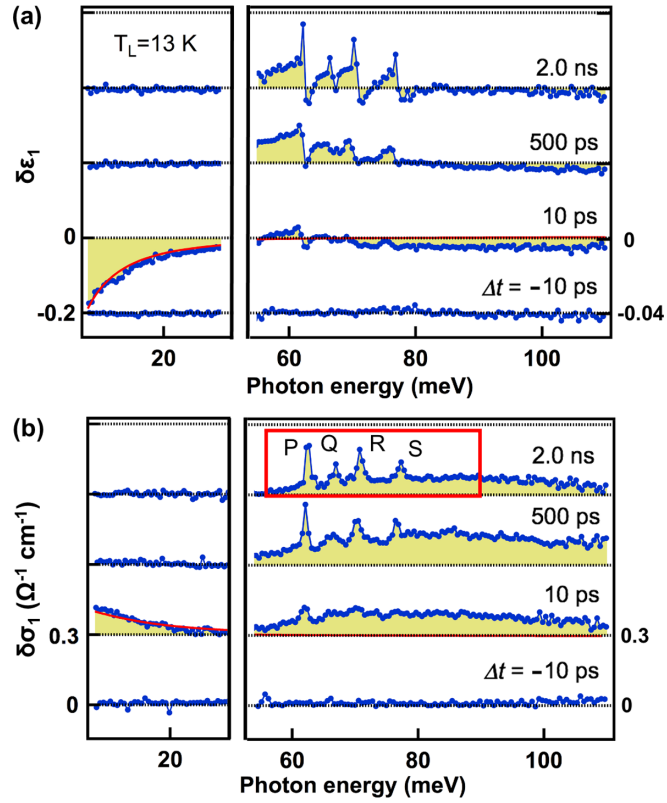

FIG. 2. Photo-induced changes in (a) relative dielectric function and (b) conductivity of diamond at lattice temperature $T_L = 13$ K after the deep ultraviolet (DUV) pulse excitation. The red solid line represents the result of Drude fitting. At $\Delta t = 2.0$ ns, four sharp peaks labeled P–S are observed (red frame). The photon energy region 30–55 meV has been omitted due to the strong absorption of Ge cryostat window.

[26] and electron-hole droplets [27], are expected. We also observed a broadband at 70 meV in $\delta\sigma_1$, attributed to the Lyman transitions of excitons. Therefore, the transformation from free carriers to excitons starts at $\Delta t = 10$ ps. At $\Delta t = 500$ ps, we observed a decrease in the Drude response and an increase in the excitonic response with four sharp peaks. The peaks show further spectral narrowing at the maximum delay time $\Delta t = 2.0$ ns. The cooling of the *e-h* equilibrium state toward the lattice temperature is completed within a subnanosecond timescale [28,29]. Therefore, the carrier temperature should be the same as the lattice temperature at 13 K with $\Delta t = 2.0$ ns. We note that $\Delta t = 2.0$ ns is considerably shorter than the lifetime of indirect excitons in diamond [30]. Here, the lowest 1*S* level EX_1 has an energy separation of 3.5 meV (~40 K) to the second lowest 1*S* level of EX_2 (Fig. S1(a) in the Supplemental Material [31]). Following the Boltzmann distribution at 13 K, a considerable number of excitons are populated at the lowest 1*S* level (Fig. S1(b) in the Supplemental Material [31]). Thus, the four observed peaks are attributed to energy splitting in the 2*P* states. Using Fermi's golden rule, the contribution of the internal transitions to the conductivity is expressed as

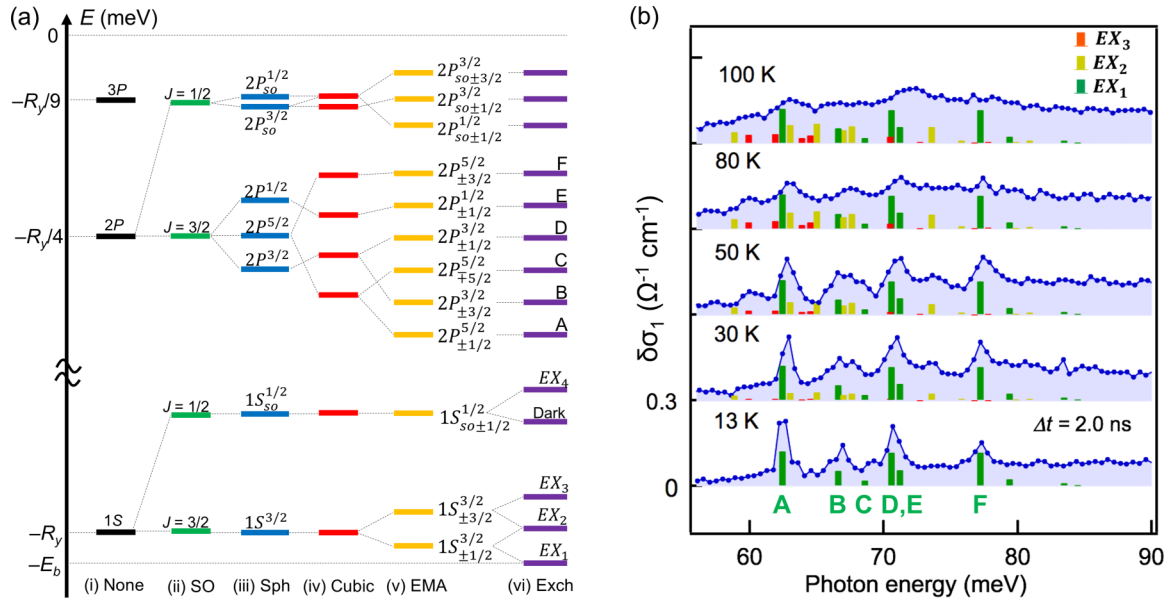

FIG. 3. (a) Schematic of the energy splitting of the $2P$ and $1S$ states, by addition of (ii) spin-orbit interaction, (iii) spherical term, (iv) cubic term, (v) electron mass-anisotropy, and (vi) exchange interaction. (b) Temperature variation of the photo-induced change in conductivity at $\Delta t = 2.0$ ns in the region surrounded by the red frame in Fig. 2(b). For comparison, calculated oscillator strengths of internal transitions from $EX_{i=1,2,3}$ to the $2P$ states labeled A–F are shown by bars.

follows [32]:

$$\delta\sigma_1(\omega) = \frac{2n_{\rm ex}e^2\omega_{\rm ex}^{(i)}|\langle\psi_{2P}|\hat{x}|\psi_{EX_1}\rangle|^2}{\hbar} \frac{\omega^2\gamma_{\rm ex}}{\left[\omega^2 - \omega_{\rm ex}^{(i)2}\right]^2 + \omega^2\gamma_{\rm ex}^2}, \tag{3}$$

where $n_{\rm ex}$ is the exciton density at the lowest $1S$ level of EX_1, $\gamma_{\rm ex}$ is the phenomenological broadening parameter, and $\omega_{\rm ex}^{(i)}$ is the transition frequency ($i = 1$–6). Here, ψ_{EX_1} and ψ_{2P} denote the wave functions of the initial $1S$ and final $2P$ states of excitons, respectively, which are calculated as the eigenfunctions of $H_{\rm ex}$ in Eq. (1). In the following, we calculate $\omega_{\rm ex}^{(i)}$ and the matrix elements in Eq. (1) based on the effective-mass approach developed by Lipari and Altarelli [8].

B. Signature of the rotational symmetry breaking of indirect excitons

We now explain the splitting in the $2P$ states using Eq. (1). First, we consider $H_{\rm so}$, leading to splitting into a doublet labeled $J = \frac{1}{2}$ and $\frac{3}{2}$ in Fig. 3(a)(ii). We focus on the $J = \frac{3}{2}$ band, which is more important in the Lyman spectra with transitions keeping J, from the $J = \frac{3}{2}$ $1S$ ground state. Including L of the envelope function, we define the total angular momentum $F = L + J$ and label the $2P$ states with F and its z component F_z as $2P^F_{F_z}$. For the $2P$ levels with $L = 1$, F takes the values of $\{\frac{1}{2}, \frac{3}{2}, \frac{5}{2}\}$ for the $J = \frac{3}{2}$ band. Because of the SO(3) symmetry of $H_{\rm sph}$, F is conserved, and the $2P^F_{F_z}$ states split into three levels of $F = \frac{1}{2}$, $\frac{3}{2}$, and $\frac{5}{2}$ [Fig. 3(a)(iii)]. However, F is not conserved under the O_h symmetry of $H_{\rm cubic}$. This causes splitting in $2P^{F=5/2}$ with respect to the absolute value of F_z [33] [Fig. 3(a)(iv)]. When we consider $H_{\rm EMA}$, futher splitting occurs by the symmetry reduction to D_{4h}, which is a subgroup of O_h symmetry of the valence band and $D_{\infty h}$ symmetry of the single conduction band valley [Fig. 3(a)(v)]. This interaction also induces significant mixing between the $2P^F_{F_z}$ levels. Therefore, we labeled the six levels by the most significant component of the envelope function. Finally, the splitting by the exchange interaction for the $2P$ levels is negligible [19], and we obtained the six $2P$ levels (A–F) for the $J = \frac{3}{2}$ band [Fig. 3(a)(vi)]. Figure 2(b) shows that the $2P$ states with $J = \frac{3}{2}$ split into four or more levels, which does not occur under SO(3) symmetry [Fig. 3(a)(iii)]. Therefore, we successfully observed the rotational symmetry breaking of excitons in indirect semiconductors. We performed the same procedure for the $1S$ states and the $2P$ states with the $J = \frac{1}{2}$ band labeled $2P^F_{{\rm so}F_z}$ [13].

We assign the four peaks in Fig. 2(b) to the Lyman transitions from EX_1 to the $2P$ states in Fig. 3(a)(vi). For a quantitative comparison, we calculated the eigenvalues and eigenfunctions of $H_{\rm ex}$ [Eq. (1)] by using $\Delta H_{\rm ex} = H_{\rm so} + H_{\rm sph} + H_{\rm cubic} + H_{\rm EMA}$ as the perturbation term and hydrogenic wave functions as nonperturbation bases. For the unknown parameters of R_y and $E_{\rm so}$ in Eq. (1), we used the typical value of the excitonic binding energy 80 meV [12] and 9.7 meV [33], respectively. Then we obtained the eigenenergies for $2P$ states and the squared matrix elements $|\langle\psi_{2P}|\hat{x}|\psi_{EX_1}\rangle|^2$ of the transitions from EX_1 to the six $2P$ levels (A–F) with $J = \frac{3}{2}$ and three $2P$ levels with $J = \frac{1}{2}$ using the solved eigenfunctions. The detailed procedure is shown in Appendices B and C. We found that the transition from EX_1 to C has the relatively small matrix element, and the energy separation between D and E was miniscule. In addition, the transitions to the three $2P$ levels with $J = \frac{1}{2}$ have much smaller oscillator strengths because the Lyman transitions occur with keeping J. Therefore, the observed four peaks are assigned to the transitions from EX_1 to A, B, {D, E}, and F. The transitions to $3P$ states are not observed because of the tiny matrix elements (see Supplemental Material [31]).

C. Significance of valence and conduction band anisotropy on the level splitting for 2*P* states

According to our level assignment in the previous subsection, the maximum energy separation measured between the highest and lowest $2P$ levels with $J = \frac{3}{2}$ is 14.9 meV, comparable with the binding energy of 20 meV in the Rydberg $2P$ state when $R_y = 80$ meV is assumed. This result indicates significant deviations in the $2P$ states from the Rydberg series. We evaluated the contribution of each $H_{\rm sph}$, $H_{\rm cubic}$, and $H_{\rm EMA}$ to the deviations. The values of $\frac{2}{n^2}\mu$, $\frac{2}{n^2}\delta$, and $\frac{2}{n^2}\mu_{01}$ ($n = 2, 3, 4, ...$) could be used as index parameters for the evaluation, which approximately corresponds to the maximum energy separation for nP states with $J = \frac{3}{2}$ in units of R_y by the respective Hamiltonians (Ref. [8] and Appendix B). For diamond, the coefficients are obtained as $\mu = 0.094$, $\delta = 0.205$, and $\mu_{01} = 0.186$, with Luttinger parameters $\gamma_1 = 2.67$, $\gamma_2 = -0.40$, $\gamma_3 = 0.68$, and the translational and longitudinal electron effective masses $m_t = 0.28m_0$ and $m_l = 1.56m_0$ [18]. Because the values of δ and μ_{01} are comparable with each other and twice as large as μ, the observed splitting for $2P$ states can be primarily attributed to the rotational symmetry breaking by $H_{\rm cubic}$ and $H_{\rm EMA}$. Moreover, based on the perturbation theory, we evaluated the contribution of $H_{\rm sph}$, $H_{\rm cubic}$, and $H_{\rm EMA}$ to the $2P$ levels and found that the maximum energy separation reduces to 12.6, 6.2, and 7.8 meV, respectively, after removing either of $H_{\rm sph}$, $H_{\rm cubic}$, and $H_{\rm EMA}$ from Eq. (1). The comparable contributions of the valence and conduction band anisotropies are specific in indirect semiconductors, leading to a significant deviation compared with the case of the direct semiconductor of cuprous oxide, where separation by the cubic term is ~3 meV, which is obtained using $R_y = 87$ meV and the parameters in Ref. [11], in the $2P$ levels. We also note that peak R is stronger than peak Q in Fig. 2(b). This situation is opposite to the case for an isotropic conduction band, where the third highest level $2P^{F=3/2}$ has a higher degeneracy than the second highest level $2P^{F=1/2}$ [Fig. 3(a)(iv)], demonstrating the crucial role of the $H_{\rm EMA}$ term.

D. Determination of the values of R_y and E_b

The assignment of the four peaks helps refining the values of R_y and E_b. The transition energies for the A and {D, E} peaks were calculated as E_b–$R_y/4$–$(0.1220 \pm 0.0005)R_y$ and E_b–$R_y/4$–$(0.0226 \pm 0.0035)R_y$, respectively, for the given value of $E_{\rm so} = 9.7$ meV [33] (Appendix B). The error comes from the uncertainty of $E_{\rm so}$ for the $2P$ states [33]. Comparison with the peak positions of P at 62.4 meV and R at 70.7 meV in Fig. 2(b) results in $R_y = 83.5 \pm 2.9$ meV and $E_b = 93.3 \pm 2.0$ meV. Using these values, the photon energies for the Lyman transitions to the $2P$ levels $\hbar\omega_{\rm ex} = E_b + E_{2P}$, and relative oscillator strengths $f_i^{2P} (\propto \omega_{\rm ex} |\langle \psi_{2P} | \hat{x} | \psi_{EX_1} \rangle|^2)$ were calculated (Table I). The results shown by the green bars in Fig. 3(b) elucidate the experimental ones, including the other peaks B and F.

The obtained $E_b = 93.3 \pm 2.0$ meV is consistent with our recent experimental result [14] and theoretical calculations for the binding energy for $1S$ states (Appendix B) from a separate approach, indicating the validity of the present quantitative analysis. The excitonic binding energy of diamond has been considered ~80 meV [12]. Our result shows that the value of 80 meV should correspond to R_y rather than E_b. Furthermore, the determined E_b gives an indirect bandgap of 5.497 ± 0.002 eV in diamond at 2 K, using the luminescence energy (5.262 eV) of the ground state excitons (EX_1) via a transverse optical phonon with 141 meV energy [13].

TABLE I. Theoretical calculation results of the transition energy $\hbar\omega_{\rm ex}$ and relative oscillator strength f_i^{2P} for excitonic $2P$ states with $J = \frac{3}{2}$ and $J = \frac{1}{2}$, for the given values of $R_y = 83.5$ meV, $E_b = 93.3$ meV, and $E_{\rm so} = 9.7$ meV. The symmetry corresponds to excitons without considering the spin of electron.

$2P$ level	Symmetry	Main component of wave functions	$\hbar\omega_{\rm ex}$ (meV)	f_i^{2P}
A	Δ_7	$2P^{5/2}_{\pm 1/2}$	62.4	1
B	Δ_6	$2P^{3/2}_{\pm 3/2}$	66.6	0.4
C	Δ_6	$2P^{5/2}_{\mp 5/2}$	68.6	0.1
D	Δ_7	$2P^{3/2}_{\pm 1/2}$	70.3	1.0
E	Δ_7	$2P^{1/2}_{\pm 1/2}$	71	0.4
F	Δ_6	$2P^{5/2}_{\pm 3/2}$	77.2	0.9
	Δ_7	$2P_{\rm so}{}^{3/2}_{\pm 1/2}$	79.4	0.2
	Δ_7	$2P_{\rm so}{}^{1/2}_{\pm 1/2}$	83.5	0.07
	Δ_6	$2P_{\rm so}{}^{3/2}_{\pm 3/2}$	84.5	0.003

Finally, Fig. 3(b) shows the photo-induced change in conductivity obtained at $\Delta t = 2.0$ ns at various temperatures in the region of the red frame indicated in Fig. 2(b). We observed new peaks and spectral broadening at higher temperatures. The temperature variation comes from the thermal populations in the higher $1S$ levels labeled EX_i ($i = 2, 3$) in Fig. 3(a)(vi). We calculated the thermal population ratios at each level as a function of temperature (Fig. S1(b) in the Supplemental Material [31]) and the oscillator strengths of the transitions from the higher $1S$ levels to the $2P$ levels (Appendix C). By including additional transitions [yellow and red bars in Fig. 3(b)], we successfully reproduced the photo-induced change in conductivity at elevated temperatures, validating our theoretical calculations and level assignments.

V. CONCLUSIONS

We observed significant deviations in the $2P$ levels of indirect excitons in diamond from the relativistic hydrogen model, which are attributed to the rotational symmetry breaking of not only valence band but also conduction band valleys by the cubic crystal environment. The excellent agreement between the perturbative calculations facilitated the determination of the Rydberg constant and binding energy for the ground state. Indirect excitons have a relatively long lifetime because of suppressed radiative recombination, beneficial for studying quantum many-body phases [34]. The detailed properties of the excitonic ground states are related to the stability of quantum many-body states through scattering processes [3,35]. Meanwhile, the quantitative analysis for the $2P$ states in this paper can be extended to states with $n \geqslant 3$. Higher excitonic states with broken rotational symmetry can exhibit unique phenomena beyond hydrogen, such as the breaking of all antiunitary symmetries in external fields [36] and a quantum-to-classical transition of chaos [4].

ACKNOWLEDGMENTS

The authors would like to thank Y. Hazama for valuable discussions. This paper was supported by a Grant-in-Aid for Scientific Research (S) (Grants No. 17H06124 and No. 21H05017), JST ACCEL (Grant No. JPMJMI17F2), a Grant-in-Aid for Scientific Research (B) (Grant No. 17H02910), and a Grant-in-Aid for Challenging Research (Exploratory) (Grant No. 19K21849) from JSPS, Japan.

APPENDIX A: MATRIX FORM OF EFFECTIVE-MASS HAMILTONIAN FOR INDIRECT EXCITONS

The matrix elements of Eq. (1), where the bases were considered in the order of $\{|J=\frac{3}{2}, J_z=\frac{3}{2}\rangle, |J=\frac{3}{2}, J_z=\frac{1}{2}\rangle, |J=\frac{3}{2}, J_z=-\frac{1}{2}\rangle, |J=\frac{3}{2},\ J_z=-\frac{3}{2}\rangle, |J=\frac{1}{2}, J_z=\frac{1}{2}\rangle, |J=\frac{1}{2}, J_z=-\frac{1}{2}\rangle\}$, are expressed as [22]

$$H_{\rm ex} = H_0 + \Delta H,$$

where $H_0 = PI$ (I: identity matrix) and

$$\Delta H = \begin{bmatrix} K+Q & L & M & 0 & \frac{i}{\sqrt{2}}L & -i\sqrt{2}M \\ L^* & K-Q & 0 & M & -i\sqrt{2}Q & i\sqrt{3/2}L \\ M^* & 0 & K-Q & -L & -i\sqrt{3/2}L^* & -i\sqrt{2}Q \\ 0 & M^* & -L^* & K+Q & -i\sqrt{2}M^* & -\frac{i}{\sqrt{2}}L^* \\ -\frac{i}{\sqrt{2}}L^* & i\sqrt{2}Q & i\sqrt{3/2}L & i\sqrt{2}M & K+E_{\rm so} & 0 \\ i\sqrt{2}M^* & -i\sqrt{3/2}L^* & i\sqrt{2}Q & \frac{i}{\sqrt{2}}L & 0 & K+E_{\rm so} \end{bmatrix}.$$

Here,

$$P = \frac{p^2}{2\mu_{\rm ex}} - \frac{e^2}{4\pi\epsilon_r\epsilon_0 r}, \quad K = \frac{p_x^2+p_y^2-2p_z^2}{2\mu_{\rm ex}}\mu_{01}, \quad Q = \frac{p_x^2+p_y^2-2p_z^2}{2\mu_{\rm ex}}\frac{(5\mu-6\delta)}{10},$$
$$L = -i\frac{(p_x-ip_y)p_z}{2\mu_{\rm ex}}\frac{2\sqrt{3}(5\mu+4\delta)}{10}, \quad M = \sqrt{3}\frac{p_x^2-p_y^2}{2\mu_{\rm ex}}\frac{(5\mu-6\delta)}{10} - i\frac{p_xp_y}{2\mu_{\rm ex}}\frac{2\sqrt{3}(5\mu+4\delta)}{10},$$

where $E_{\rm so} = \bar{\Delta}R_y$, and ϵ_r and ϵ_0 are the relative permittivity of diamond and the vacuum permittivity, respectively. Parameters of $\mu_{\rm ex}$, μ, δ, and μ_{01} are defined in Sec. II of the main text. Component K is obtained from the mass anisotropy effect in the conduction band. Here, L, M, and Q are acquired from hole dispersion. Further, ΔH includes the spin-orbit interactions, spherical term, cubic term, and electron mass anisotropy [Eq. (1)] and is treated as a perturbation term.

APPENDIX B: BINDING ENERGIES OF EXCITONIC 2*P* AND 1*S* STATES

To solve the Schrödinger equations corresponding to the Hamiltonian equation [Eq. (1)] by the perturbation approach, we define the eigenwave functions for the exciton states following the L-S coupling scheme used for atomic systems. We use the F and F_z representations, where $F = L + J$ is the sum of the angular momentum L of the envelope function, and the pseudo-angular momentum J corresponds to the valence band. We consider the excitonic $2P$ states with $L = 1$. The wave functions can be expanded as [8]

$$|\psi_{\rm ex}(\vec{r})\rangle = \sum_i f_{2P}(r)|L=1,\ J, F_i, F_{zi}\rangle|e\rangle,$$

where $f_{2P}(r)$ represents the radial function of the Rydberg $2P$ state. The electron spin $|e\rangle$ corresponds to the up or down spins. Because the exchange interaction is negligible for the $2P$ states, the energy levels are degenerate for the up and down spins. Thus, we omit $|e\rangle$ in the following and rewrite $f_{2P}(r)|L=1, J=\frac{3}{2}, F, F_z\rangle$ as $2P^F_{F_z}$. When we consider the $2P$ states originating from the heavy and light valence bands ($J=\frac{3}{2}$), there are 12 eigen functions $2P^{1/2}_{\pm1/2}$, $2P^{3/2}_{\pm1/2}$, $2P^{5/2}_{\pm1/2}$, $2P^{3/2}_{\pm3/2}$, $2P^{5/2}_{\pm3/2}$, and $2P^{5/2}_{\mp5/2}$. These are classified into two groups: $\{2P^{1/2}_{\pm1/2}, 2P^{3/2}_{\pm1/2}, 2P^{5/2}_{\pm1/2}\}$ with symmetry Δ_7 and $\{2P^{3/2}_{\pm3/2}, 2P^{5/2}_{\pm3/2}, 2P^{5/2}_{\mp5/2}\}$ with symmetry Δ_6. Concerning the $2P$ states generated from the split-off band ($J=\frac{1}{2}$), the six eigenfunctions are represented as $2P_{{\rm so}\pm1/2}{}^{3/2}$, $2P_{{\rm so}\pm1/2}{}^{1/2}$, and $2P_{{\rm so}\pm3/2}{}^{3/2}$, which have the symmetries Δ_7, Δ_7, and Δ_6, respectively. We calculated the matrix elements of the Hamiltonian, where the unperturbed bases were ordered as $2P^{1/2}_{\pm1/2}$, $2P^{3/2}_{\pm1/2}$, $2P^{5/2}_{\pm1/2}$, $2P_{{\rm so}\pm1/2}{}^{3/2}$, $2P_{{\rm so}\pm1/2}{}^{1/2}$, $2P^{3/2}_{\pm3/2}$, $2P^{5/2}_{\pm3/2}$, $2P^{5/2}_{\mp5/2}$, and $2P_{{\rm so}\pm3/2}{}^{3/2}$.

Consequently,

$$\Delta H^{2P} = \int \left(2P^F_{F_z}\right)^* \Delta H \left(2P^F_{F_z}\right) d\vec{r}$$

$$= \begin{bmatrix} \frac{\mu}{4} & \mp\frac{\mu_{01}}{10\sqrt{5}} & \frac{3\mu_{01}}{10\sqrt{5}} & -i\frac{\mu}{3} & \mp i\frac{\mu}{6\sqrt{2}} \\ \mp\frac{\mu_{01}}{10\sqrt{5}} & -\frac{1}{5}\left(\mu-\frac{2}{5}\mu_{01}\right) & \pm\frac{3}{50}(2\delta+\mu_{01}) & \mp i\frac{\mu}{12\sqrt{5}} & i\frac{\mu}{3\sqrt{10}} \\ \frac{3\mu_{01}}{10\sqrt{5}} & \pm\frac{3}{50}(2\delta+\mu_{01}) & -\frac{1}{20}\left(-\mu+\frac{12}{5}\delta+\frac{8}{5}\mu_{01}\right) & -i\frac{\delta}{5\sqrt{5}} & \pm i\frac{2\sqrt{2}\delta}{5\sqrt{5}} \\ +i\frac{\mu}{3} & \pm i\frac{\mu}{12\sqrt{5}} & +i\frac{\delta}{5\sqrt{5}} & \bar{\Delta}-\frac{\mu_{01}}{10} & -\frac{\mu_{01}}{5\sqrt{2}} \\ \pm i\frac{\mu}{6\sqrt{2}} & -i\frac{\mu}{3\sqrt{10}} & \mp i\frac{2\sqrt{2}\delta}{5\sqrt{5}} & -\frac{\mu_{01}}{5\sqrt{2}} & \bar{\Delta} \end{bmatrix}$$

$$\begin{bmatrix} -\frac{1}{5}\left(\mu+\frac{2}{5}\mu_{01}\right) & \mp\frac{\sqrt{6}}{50}(\delta-3\mu_{01}) & \mp\frac{\sqrt{30}}{50}\delta & \mp i\frac{\mu}{4\sqrt{5}} \\ \mp\frac{\sqrt{6}}{50}(\delta-3\mu_{01}) & -\frac{1}{100}(-5\mu+2\mu_{01}-18\delta) & -\frac{3\sqrt{5}\delta}{50} & +i\frac{\sqrt{30}\delta}{50} \\ \mp\frac{\sqrt{30}}{50}\delta & -\frac{3\sqrt{5}}{50}\delta & -\frac{1}{100}(-5\mu-10\mu_{01}+6\delta) & +i\frac{\sqrt{6}\delta}{10} \\ \pm i\frac{\mu}{4\sqrt{5}} & -i\frac{\sqrt{30}\delta}{50} & -i\frac{\sqrt{6}\delta}{10} & \bar{\Delta}+\frac{\mu_{01}}{10} \end{bmatrix}$$

in units of R_y. For given values of $\gamma_1 = 2.67$, $\gamma_2 = -0.40$, $\gamma_3 = 0.68$, $m_t = 0.28\,m_0$, and $m_l = 1.56\,m_0$ [18], the coefficients are calculated as $\mu = 0.094$, $\delta = 0.205$, and $\mu_{01} = 0.186$, which are comparable with those in silicon, where the mass anisotropy effect can be treated as a perturbation [8].

The maximum energy separations for the nP states with $J = \frac{3}{2}$ by the spherical, cubic, and electron mass anisotropy terms, respectively, are obtained by calculating the eigenvalues of $\Delta H^{nP} = \int (nP^F_{F_z})^*\, \Delta H (nP^F_{F_z})\, d\vec{r}$. When the spin-orbit interaction is considerably larger than the excitonic binding energy ($\bar{\Delta} = E_{\rm so}/R_y \to \infty$), as in many semiconductors, the matrix elements of the Hamiltonian, where the unperturbed bases are taken in the order of $2P^{1/2}_{\pm1/2}$, $2P^{3/2}_{\pm1/2}$, $2P^{5/2}_{\pm1/2}$, $2P^{3/2}_{\pm3/2}$, $2P^{5/2}_{\pm3/2}$, and $2P^{5/2}_{\mp5/2}$, is described as

$$\delta H^{nP} = \frac{4}{n^2} \begin{bmatrix} \frac{\mu}{4} & \mp\frac{\mu_{01}}{10\sqrt{5}} & \frac{3\mu_{01}}{10\sqrt{5}} \\ \mp\frac{\mu_{01}}{10\sqrt{5}} & -\frac{1}{5}\left(\mu-\frac{2}{5}\mu_{01}\right) & \pm\frac{3}{50}(2\delta+\mu_{01}) \\ \frac{3\mu_{01}}{10\sqrt{5}} & \pm\frac{3}{50}(2\delta+\mu_{01}) & -\frac{1}{20}\left(-\mu+\frac{12}{5}\delta+\frac{8}{5}\mu_{01}\right) \end{bmatrix}$$

$$\begin{bmatrix} -\frac{1}{5}\left(\mu+\frac{2}{5}\mu_{01}\right) & \mp\frac{\sqrt{6}}{50}(\delta-3\mu_{01}) & \mp\frac{\sqrt{50}}{50}\delta \\ \mp\frac{\sqrt{6}}{50}(\delta-3\mu_{01}) & -\frac{1}{100}(-5\mu+2\mu_{01}-18\delta) & -\frac{3\sqrt{5}}{50}\delta \\ \mp\frac{\sqrt{30}}{50}\delta & -\frac{3\sqrt{5}}{50}\delta & -\frac{1}{100}(-5\mu-10\mu_{01}+6\delta) \end{bmatrix}.$$

The maximum energy separation by each $H_{\rm sph}$, $H_{\rm cubic}$, and $H_{\rm EMA}$ for nP states with $J = \frac{3}{2}$ is $\frac{9}{20}\mu\frac{4}{n^2}(= 0.45\mu\frac{4}{n^2})$, $\frac{(15+3\sqrt{5})}{50}\delta\frac{4}{n^2}(= 0.43\delta\frac{4}{n^2})$, and $\frac{3}{10}\mu_{01}\frac{4}{n^2}(= 0.3\mu_{01}\frac{4}{n^2})$, respectively, which can be written approximately as $\frac{2}{n^2}\mu$, $\frac{2}{n^2}\delta$, and $\frac{2}{n^2}\mu_{01}$ in units of R_y.

Next, we consider all terms of $H_{\rm so}$, $H_{\rm sph}$, $H_{\rm cubic}$, and $H_{\rm EMA}$. By setting $E_{\rm so} = 9.7$ meV, we calculated the eigenenergy E_{2P} of the six $2P$ levels (A–F) based on the second-order degenerate perturbation theory. In the analysis, we included the coupling of hydrogenlike and continuum states with $n \geqslant 2$ [8,22]. We considered the uncertainty of the value of $E_{\rm so}$ between 8.6 and 10.8 meV [34] for the $2P$ states, and the energies were defined as the averages of the two boundary results. Table II lists the resultant E_{2P} for the typical value of the excitonic binding energy of $R_y = 80$ meV. Table I shows the photon energies of Lyman transitions for the given value of $R_y = 83.5$ meV determined from energy positions of peaks P and R in Fig. 2(b).

TABLE II. Theoretical calculation results of the binding energy E_{2P} and squared matrix element for excitonic $2P$ states with $J = \frac{3}{2}$ and $J = \frac{1}{2}$, for the given values of $R_y = 80$ meV and $E_{\rm so} = 9.7$ meV. The symmetry corresponds to excitons without considering the spin of electron.

$2P$ level	Symmetry	Main component of wave functions	E_{2P} (meV)	Squared matrix element
A	Δ_7	$2P^{5/2}_{\pm1/2}$	−29.7	1
B	Δ_6	$2P^{3/2}_{\pm3/2}$	−25.7	0.4
C	Δ_6	$2P^{5/2}_{\mp5/2}$	−23.8	0.1
D	Δ_7	$2P^{3/2}_{\pm1/2}$	−21.9	0.9
E	Δ_7	$2P^{1/2}_{\pm1/2}$	−21.3	0.3
F	Δ_6	$2P^{5/2}_{\pm3/2}$	−15.6	0.8
	Δ_7	$2P_{{\rm so}\pm1/2}^{3/2}$	−13.5	0.2
	Δ_7	$2P_{{\rm so}\pm1/2}^{1/2}$	−9.6	0.06
	Δ_6	$2P_{{\rm so}\pm3/2}^{3/2}$	−8.6	0.003

TABLE III. Calculation results of the binding energy for excitonic $1S$ states. The symmetry corresponds to excitons without considering the spin of electron.

Symmetry	$1S$ level	Binding energy (meV)
Δ_7	$1S^{3/2}_{\pm3/2}$	91.2
Δ_6	$1S^{3/2}_{\pm1/2}$	94.6

TABLE IV. Calculation results of the relative oscillator strength of the transition from EX_2 and EX_3 to excitonic nine $2P$ states, for the given values of $R_y = 83.5$ meV, $E_b = 93.3$ meV, and $E_{so} = 9.7$ meV.

$2P$ level	Main component of wave functions	Oscillator strength of the transition from EX_2 (relative unit)	Oscillator strength of the transition from EX_3 (relative unit)
A	$2P^{5/2}_{\pm 1/2}$	0.51	0.28
B	$2P^{3/2}_{\pm 3/2}$	0.85	0.60
C	$2P^{5/2}_{\mp 5/2}$	0.91	0.68
D	$2P^{3/2}_{\pm 1/2}$	0.61	0.36
E	$2P^{1/2}_{\pm 1/2}$	0.79	0.56
F	$2P^{5/2}_{\pm 3/2}$	0.74	0.47
	$2P_{so}{}^{3/2}_{\pm 1/2}$	0.12	0.07
	$2P_{so}{}^{1/2}_{\pm 1/2}$	0.04	0.02
	$2P_{so}{}^{3/2}_{\pm 3/2}$	0.11	0.08

The $1S$ state splits into two levels with Δ_6 and Δ_7 symmetry. The energy shifts are described as [8]

$$\Delta E_{1S} = \left[\frac{4}{25}(24\delta^2+25\mu^2)+\frac{16}{5}{\mu_{01}}^2 \pm \frac{16}{5}\mu_{01}(10\mu-12\delta)\right] \times S_1(0) + \frac{4}{25}(24\delta^2+25\mu^2)S_1(\overline{\Delta}),$$

where $S_1(x) = \sum_{n=3}^{\infty} \frac{|I_n|^2}{x+1-1/n^2} + \int_0^{\infty} \frac{|I_k|^2}{x+1-1/k^2} dk$, $I_n = \int_0^{\infty} R_{n2}(r)(r+r^2)e^{-r}dr$, and $R_{nl}(r)$ represent the normalized hydrogenic radial wave functions. The (+) and (−) signs within the brackets apply to the Δ_6 and Δ_7 states, respectively. Table III lists the binding energies calculated assuming $\gamma_1 = 2.67$, $\gamma_2 = -0.40$, $\gamma_3 = 0.68$, $E_{so} = 9.7$ meV [33], and $R_y = 83.5$ meV [37]. The theoretically calculated value of E_b, 94.6 meV, is consistent with the experimentally estimated value of 93.3 meV ± 2.0 meV within the error.

APPENDIX C: OSCILLATOR STRENGTHS OF THE TRANSITIONS FROM 1S TO 2P STATES

Previously in Ref. [13], the Hamiltonian ΔH^{1S} for the excitonic $1S$ states was derived to calculate $|\psi_{EX_1}\rangle$. Here, the calculation was performed under simplified conditions that the masses of the valence and conduction bands exhibit no anisotropy, the split-off and other valence bands are not mixed, and the effective masses for valence bands are all the same. Here, EX_1 consists of doublet Δ_5 and nondegenerate Δ_4 states. The wave functions for the Δ_5 and Δ_4 states, which diagonalize ΔH^{1S} with this simplified condition, are $\{\frac{1}{2}(\phi^8_{-1/2}\uparrow + \sqrt{3}\phi^8_{-3/2}\downarrow)$, $\frac{1}{2}(\sqrt{3}\phi^8_{3/2}\uparrow + \phi^8_{1/2}\downarrow)\}$, and $\frac{1}{\sqrt{2}}(\phi^8_{-3/2}\uparrow - \phi^8_{+3/2}\downarrow)$, respectively. We calculated squared matrix elements $|\langle\psi_{2P}|\hat{x}|\psi_{EX_1}\rangle|^2$ of the internal transitions to the $2P$ states (A–F) from EX_1, for the values of $R_y = 83.5$ and 80 meV. Tables I and II present the results.

We also calculated the squared matrix elements of $|\langle\psi_{2P}|\hat{x}|\psi_{EX_{2,3}}\rangle|^2$ and the relative oscillator strengths of the transitions from EX_2 and EX_3 to the $2P$ states. The wave functions are approximately described as $\{\phi^8_{1/2}\uparrow, \phi^8_{-1/2}\downarrow, \frac{1}{\sqrt{2}}(\phi^8_{-3/2}\uparrow + \phi^8_{+3/2}\downarrow)\}$ for EX_2 and $\{\frac{1}{2}(\sqrt{3}\phi^8_{-1/2}\uparrow - \phi^8_{-3/2}\downarrow)$ and $\frac{1}{2}(-\phi^8_{3/2}\uparrow + \sqrt{3}\,\phi^8_{1/2}\downarrow)\}$ for EX_3 [13]. Table IV lists the calculated values of the relative oscillator strengths for $E_{so} = 9.7$ meV and $R_y = 83.5$ meV.

[1] G. H. Wannier, Phys. Rev. **52**, 191 (1937).
[2] T. Kazimierczuk, D. Fröhlich, S. Scheel, H. Stolz, and M. Bayer, Nature (London) **514**, 343 (2014).
[3] K. Yoshioka, E. Chae, and M. Kuwata-Gonokami, Nat. Commun. **2**, 328 (2011).
[4] M. Aßmann, J. Thewes, D. Fröhlich, and M. Bayer, Nat. Mater. **15**, 741 (2016).
[5] V. Fock, Z. Phys. **98**, 145 (1935).
[6] W. E. Lamb and R. C. Retherford, Phys. Rev. **72**, 241 (1947).
[7] A. K. Ramdas and S. Rodriguez, Rep. Prog. Phys. **44**, 1297 (1981).
[8] N. O. Lipari and M. Altarelli, Phys. Rev. B **15**, 4883 (1977).
[9] D. Labrie, M. L. W. Thewalt, I. J. Booth, and G. Kirczenow, Phys. Rev. Lett. **61**, 1882 (1988).
[10] T. Timusk, Phys. Rev. B **13**, 3511 (1976).
[11] J. Thewes, J. Heckötter, T. Kazimierczuk, M. Aßmann, D. Fröhlich, M. Bayer, M. A. Semina, and M. M. Glazov, Phys. Rev. Lett. **115**, 027402 (2015).
[12] P. J. Dean, E. C. Lightowlers, and D. R. Wight, Phys. Rev. **140**, A352 (1965).
[13] Y. Hazama, N. Naka, and H. Stolz, Phys. Rev. B **90**, 045209 (2014).
[14] T. Ichii, Y. Hazama, N. Naka, and K. Tanaka, Appl. Phys. Lett. **116**, 231102 (2020).
[15] T. Tayagaki, A. Mysyrowicz, and M. Kuwata-Gonokami, Phys. Rev. B **74**, 245127 (2006).
[16] M. Kubouchi, K. Yoshioka, R. Shimano, A. Mysyrowicz, and M. Kuwata-Gonokami, Phys. Rev. Lett. **94**, 016403 (2005).
[17] G. F. Koster, J. O. Dimmock, R. G. Wheeler, and H. Statz, *Properties of the Thirty-Two Point Groups* (MIT Press, Cambridge, MA, 1963).
[18] N. Naka, K. Fukai, Y. Handa, and I. Akimoto, Phys. Rev. B **88**, 035205 (2013).
[19] Y. Toyozawa, *Optical Processes in Solids* (Cambridge University Press, Cambridge, UK, 2003).
[20] G. Dresselhaus, J. Phys. Chem. Solids **1**, 14 (1956).

[21] J. M. Luttinger and W. Kohn, Phys. Rev. **97**, 869 (1955).
[22] N. O. Lipari and A. Baldereschi, Phys. Rev. B **3**, 2497 (1971).
[23] N. Naka, T. Kitamura, J. Omachi, and M. Kuwata-Gonokami, Phys. Status Solidi B **245**, 2676 (2008).
[24] J. Dai, N. Karpowicz, and X. C. Zhang, Phys. Rev. Lett. **103**, 023001 (2009).
[25] J. Dai, X. Xie, and X. C. Zhang, Phys. Rev. Lett. **97**, 103903 (2006).
[26] J. Omachi, T. Suzuki, K. Kato, N. Naka, K. Yoshioka, and M. Kuwata-Gonokami, Phys. Rev. Lett. **111**, 026402 (2013).
[27] M. Nagai, R. Shimano, K. Horiuchi, and M. Kuwata-Gonokami, Phys. Rev. B **68**, 081202(R) (2003).
[28] T. Suzuki and R. Shimano, Phys. Rev. B **83**, 085207 (2011).
[29] A. Hangleiter, Z. Jin, M. Gerhard, D. Kalincev, T. Langer, H. Bremers, U. Rossow, M. Koch, M. Bonn, and D. Turchinovich, Phys. Rev. B **92**, 241305(R) (2015).
[30] N. Naka, H. Morimoto, and I. Akimoto, Phys. Status Solidi A **213**, 2551 (2016).
[31] See Supplemental Material at http://link.aps.org/supplemental/10.1103/PhysRevB.104.205201, which includes Refs. [13,30], for calculation results of the transition energies and oscillator strengths for $3P$ states and thermal exciton populations for $1S$ states.
[32] H. Haug and S. W. Koch, *Quantum Theory of the Optical and Electronic Properties of Semiconductors* (World Scientific, Singapore, 2009).
[33] The interactions via cubic terms between different $2P$ levels give rise to the energy splitting when $\Delta F = 0$ and $\Delta F_z = \pm 4$. For the $2P$ levels with $F = \frac{5}{2}$, the interaction between $2P^{F=5/2}_{F_z=\mp 3/2}$ and $2P^{F=5/2}_{F_z=\pm 5/2}$ results in the splitting. For the $2P$ levels with $F = \frac{3}{2}$ and $\frac{1}{2}$, $\Delta F = 0$ and $\Delta F_z = \pm 4$ are not allowed, and no splitting occurs.
[34] J. Serrano, M. Cardona, and T. Ruf, Solid State Commun. **113**, 411 (2000).
[35] T. Suzuki and R. Shimano, Phys. Rev. Lett. **103**, 057401 (2009).
[36] K. Mizoo, T. J. Inagaki, Y. Ueshima, and M. Aihara, J. Phys. Soc. Japan **74**, 1745 (2005).
[37] F. Schweiner, J. Main, and G. Wunner, Phys. Rev. Lett. **118**, 046401 (2017).